





# Use of Transition Models to Design High Performance TESs for the LCLS-II Soft X-Ray Spectrometer

Kelsey M. Morgan , Dan T. Becker , Douglas Alan Bennett, William B. Doriese , Johnathon D. Gard, Kent D. Irwin, Sang Jun Lee , Dale Li, John A. B. Mates, Christine G. Pappas, Dan R. Schmidt, Charles J. Titus , Dan D. Van Winkle, Joel N. Ullom, Abigail Wessels, and Daniel S. Swetz

**Abstract**—We are designing an array of transition-edge sensor (TES) microcalorimeters for a soft X-ray spectrometer at the Linac Coherent Light Source at SLAC National Accelerator Laboratory to coincide with upgrades to the free electron laser facility. The complete spectrometer will have 1000 TES pixels with energy resolution of 0.5 eV full-width at half-maximum (FWHM) for incident energies below 1 keV while maintaining pulse decay-time constants shorter than 100  $\mu$ s. Historically, TES pixels have often been designed for a particular scientific application via a combination of simple scaling relations and trial-and-error experimentation with device geometry. We have improved upon this process by using our understanding of transition physics to guide TES design. Using the two-fluid approximation of the phase-slip line model for TES resistance, we determine how the geometry and critical temperature of a TES will affect the shape of the transition. We have used these techniques to design sensors with a critical temperature of 55 mK. The best sensors achieve an energy resolution of 0.75 eV FWHM at 1.25 keV. Building upon this result, we show how the next generation of sensors can be designed to reach our goal of 0.5 eV resolution.

**Index Terms**—Superconducting thin films, thin film sensors, x-ray detectors.

Manuscript received October 30, 2018; accepted February 26, 2019. Date of publication March 4, 2019; date of current version April 16, 2019. This work was supported in part by the U.S. Department of Energy, Office of Science, Office of Basic Energy Sciences, and in part by the NIST Innovations in Measurement Science Program. (*Corresponding author: Kelsey Morgan.*)

K. M. Morgan is with the Department of Physics, University of Colorado Boulder, Boulder, CO 80309 USA, and also with the National Institute of Standards and Technology, Boulder, CO 80305 USA (e-mail: kelsey.morgan@nist.gov).

D. T. Becker, J. D. Gard, J. A. B. Mates, and J. N. Ullom are with the Department of Physics, University of Colorado Boulder, Boulder, CO 80309 USA, and also with the National Institute of Standards and Technology, Boulder, CO 80305 USA.

D. A. Bennett, W. B. Doriese, C. G. Pappas, D. R. Schmidt, and D. S. Swetz are with the National Institute of Standards and Technology, Boulder, CO 80305 USA.

K. D. Irwin is with Stanford University, Stanford, CA 94305 USA, and also with the SLAC National Accelerator Laboratory, Menlo Park, CA 94025 USA.

C. J. Titus is with Stanford University, Stanford, CA 94305 USA.

A. Wessels is with the Department of Physics, University of Colorado Boulder, Boulder, CO 80309 USA.

D. Li, S.-J. Lee, and D. D. Van Winkle are with the SLAC National Accelerator Laboratory, Menlo Park, CA 94025 USA.

Color versions of one or more of the figures in this paper are available online at <http://ieeexplore.ieee.org>.

Digital Object Identifier 10.1109/TASC.2019.2903032

## I. INTRODUCTION

THE transition-edge sensor (TES) spectrometer has emerged as a powerful tool for x-ray science at light sources [1]. A TES array provides a combination of high resolving power and high photon collection efficiency, enabling x-ray emission and absorption measurements of weak, dilute, or radiation sensitive samples [2]. TES spectrometers have now been used successfully at beamlines at the Advanced Photon Source [3], National Synchrotron Light Source [3], and the Stanford Synchrotron Light Source at SLAC [4]. SLAC has commissioned a TES x-ray spectrometer for the upgraded Linac Coherent Light Source (LCLS-II). The spectrometer as currently specified includes a 1,000 pixel TES array that can achieve 0.5 eV full-width at half-maximum (FWHM) resolution for x-ray energies below 1 keV, and the TESs will have  $1/e$  pulse decay time constants less than 100  $\mu$ s [5].

The current generation of TES beamline spectrometers typically achieves energy resolutions of 1.2 eV-1.5 eV FWHM at 1 keV [3]. Those arrays are comprised of 120  $\mu$ m  $\times$  120  $\mu$ m Mo/Cu bilayer TESs with 3 normal-metal Cu bars (sometimes called zebra stripes) used to suppress excess noise and widen the transition [3]. The challenging energy resolution requirements for LCLS-II will require significant changes to the TES pixel design. To enable the necessary improvement, the new spectrometer will be cooled by a dilution refrigerator. The dilution refrigerator can provide a base temperature as low as 8 mK [5] and provides significantly higher cooling power for a given base temperature than can the adiabatic demagnetization refrigerators (ADRs) used to cool the beamline instruments described in Ref. [3]. This in turn allows operation of sensors with lower critical temperature ( $T_c$ ) and improved energy resolution.

However, heat capacity, thermal conductance, and the shape of the TES transition all change with temperature, so simply making the same TES design at lower  $T_c$  will produce a pixel with diminished linear range and a slower pulse decay-time constant. Therefore, the TES geometry must be altered to compensate for these temperature-dependent effects. The design/fabrication/test cycle is time consuming and expensive, so reduction of the number of fabricated wafers and the number of TES design variations that must be tested is highly desirable.

The two-fluid model gives us a way to calculate how changes in TES parameters like current and resistance change the shape of the TES transition [6], [7]. This information can be used to guide design decisions such as choosing the number of normal metal bars that might have previously required testing many

variants in a trial-and-error approach. Here, we use these techniques to design sensors that achieve 0.75 eV FWHM energy resolution at 1.25 keV with  $T_c = 55$  mK. Then, we describe the design changes needed to reduce  $T_c$  to 30 mK, which will enable the 0.5 eV FWHM resolution specified for LCLS-II.

## II. DETECTOR DESIGN FOR $T_c = 55$ MK

### A. Dependence of TES Properties on Temperature

GENERALLY, the temperature dependence of TES properties like the heat capacity and the thermal conductance are well understood. We use a 1  $\mu\text{m}$  thick  $\text{SiN}_x$  membrane to provide thermal isolation between the TES and the heat bath. The thermal conductance of this link is parameterized as  $G(T) \equiv n\kappa T^{n-1}$ , where  $\kappa$  and  $n$  can be determined from fits to I-V curves. Typically,  $n$  is expected to be between 3-4 for a TES on a thin nitride membrane [8], [9]. The heat capacity ( $C$ ) of a metal scales approximately linearly with temperature. Therefore, as  $T_c$  is reduced, both  $C$  and  $G$  will drop, but  $G$  will drop faster.

Consequently, we expect the pulse decay-time to get longer because it is proportional to  $C/G$ . This is undesirable in an environment like LCLS-II, where total flux is expected to be high and overall throughput is an important consideration. Additionally, the range over which the resistive transition is approximately linear is proportional to  $CT/\alpha$ , where  $T$  is the TES temperature and  $\alpha \equiv T/R \partial R/\partial T$  at constant TES current ( $I$ ). So, this energy range is reduced as  $T_c$  is lowered.

However, the linear range and energy resolution also depend on  $\alpha$ , which parameterizes the sharpness of the superconducting transition. Determining how, if at all,  $\alpha$  will evolve with TES geometry and temperature requires a model of the superconducting transition.

### B. Two-Fluid Model

Although much progress has been made in understanding the evolution of resistance between the superconducting and normal states in a TES, we cannot yet accurately predict the shape of the transition for an arbitrary TES geometry from first principles. A thorough review of the current theoretical understanding of the transition can be found in Ref. [2].

In some TESs, the critical current has been shown to follow a weak-link model, suggesting that the superconductivity in the film is strongly influenced by the longitudinal proximity effect induced by the superconducting leads [10]. Models treating the TES as a resistively shunted junction between the leads have shown some promise for explaining this behavior [11], [12]. Additionally, proximity effect models may provide some insight into the effect of normal-metal features such as bars and banks on the superconductivity of the bilayer [13].

In devices where weak-link effects are minimal, a phase-slip line model for the onset of resistance has been shown to be a good description of TES I-V characteristics [14]. However, applying this model to complex TES geometries makes calculations extremely difficult. Instead, we can use the two-fluid model, which is a simplified version of the Skocpol-Beasley-Tinkham model for the behavior of phase-slips [15]. The two-fluid model has been shown to be a good description of how the parameters  $\alpha$  and  $\beta$ , where  $\beta \equiv I/R \partial R/\partial I$  at constant  $T$ , evolve throughout the TES transition [6].

The two-fluid model describes the total current in a biased TES as a combination of a supercurrent and a quasiparticle

current. The resistance of the film can be written as:

$$R(V, T) = \left( \frac{c_I I_c(T)}{V} + \frac{1}{c_R R_n} \right)^{-1} \quad (1)$$

where  $c_I$  is the ratio of time-averaged critical current to the critical current, and  $c_R = 2N\rho_\lambda\Lambda_{Q^*}/R_n$ , where  $N$  is the number of phase slip lines,  $\rho_\lambda$  is the normal resistance per unit length,  $\Lambda_{Q^*}$  is the charge imbalance relaxation length, and  $R_n$  is the normal resistance [6]. Typically,  $c_I$  and  $c_R$  are treated as constants, although  $c_R$  is expected to have a weak temperature dependence and has been shown to increase slowly through the transition [16]. In large, thin films, the critical current is expected to follow the Ginsburg-Landau form:  $I_c(T) = I_{c0}(1-T/T_c)^{3/2}$ . By substituting in this expression for  $I_c(T)$  and taking partial derivatives of (1) we can derive expressions for  $\alpha$  and  $\beta$  [6]:

$$\alpha = \frac{3}{2} c_I c_R \frac{R_n I_{c0}}{R_0 I_0 T_c} \left( 1 - \frac{T_0}{T_c} \right)^{1/2} \quad (2a)$$

$$\beta = c_R \frac{R_n}{R_0} - 1 \quad (2b)$$

where  $I_{c0}$  is the zero-temperature critical current. Equations (1) and (2a) can be combined with the following equation describing the Joule power dissipation in the TES:

$$I^2 R = \kappa (T^n - T_b^n) \quad (3)$$

to calculate the TES current, temperature, and  $\alpha$  for a given bias point, assuming  $c_R$ ,  $I_{c0}$  and  $T_c$  are known.

We use these equations coupled with measurements of previous devices with  $T_c = 76$  mK to determine what design changes should be made when  $T_c$  is reduced.

### C. Scaling Previous Results

Previously, we demonstrated a Mo/Cu bilayer with lateral dimensions of 212  $\mu\text{m} \times 106 \mu\text{m}$ , four evenly spaced normal-metal Cu bars, and  $T_c = 76$  mK that achieved energy resolution of 1.02 eV FWHM at 1.25 keV [16]. The heat capacity of the TES was 0.11 pJ/K, with  $R_n = 14.5$  m $\Omega$ , and  $G = 130$  pW/K at  $T_c$  with  $n = 3.52$ . The critical current followed the Ginsburg-Landau expression for a thin film, suggesting that weak-link effects in these devices were minimal.

Heat capacity per volume decreases linearly with  $T_c$ . To compensate for the loss of linear range this causes, we can either increase the pixel size to increase  $C$ , or we can reduce  $\alpha$ . Increasing the pixel size has the benefit of providing additional collecting area. If  $T_c$  is reduced to 55 mK from 76 mK, the linear range will be reduced by  $(C(76 \text{ mK})/C(55 \text{ mK})) \times (76 \text{ mK}/55 \text{ mK}) = 1.9$ , assuming constant  $\alpha$ . Therefore, we increase the area of the pixel to 200  $\mu\text{m} \times 200 \mu\text{m}$  to compensate.

Finally, we consider how  $\alpha$  and  $\beta$  change as  $T_c$  is reduced. The energy resolution of a TES is  $\Delta E^2 \propto (CT^2/\alpha)\sqrt{(1+2\beta)}$ . If  $\alpha$  and  $\beta$  can be kept constant as  $T_c$  is reduced and the smaller heat capacity per volume is compensated by an increase in pixel size, then the linear range of the pixel will be maintained while the energy resolution improves as  $(T_{c,low}/T_{c,high})^{1/2}$ . Given this scaling, reduction of  $T_c$  to 55 mK will not be sufficient to achieve our goal of  $\Delta E = 0.5$  eV; however,  $T_c = 55$  mK was the lowest we could test in the available cryogenic platform, which

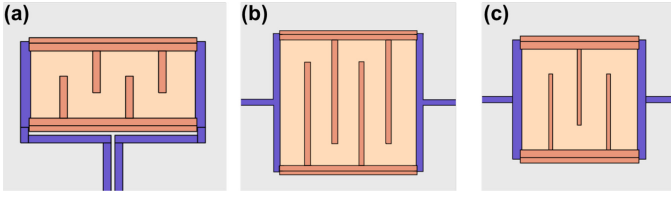


Fig. 1. The TES devices described in this work were composed of a Mo/Cu bilayer (light orange) suspended on a SiN<sub>x</sub> membrane (gray) with superconducting Mo leads (blue). Cu banks on the edges of the devices prevented superconducting shorts, and varying numbers of perpendicular Cu bars were added across the devices (dark orange). (a) A 212 μm × 106 μm device with 4 Cu bars with  $T_c = 76$  mK. A 3 μm-thick layer of bismuth was deposited on top of the device to increase x-ray absorption efficiency (not pictured). (b) A 200 μm × 200 μm device with 4 Cu bars,  $T_c = 54.5$  mK, and a 1.1 μm-thick Bi absorbing layer (not pictured). (c) A 180 μm × 180 μm device with 3 Cu bars,  $T_c = 54.5$  mK, and a 1.1 μm-thick Bi absorbing layer (not pictured).

provided a minimum  $T_{bath} = 35$  mK (the energy resolution will degrade as  $T_{bath}$  approaches  $T_c$ ).

According to the two-fluid model,  $\beta$  is approximately constant for fixed bias point ( $R/R_n$ ). However,  $\alpha$  depends on the bias current, which will change for fixed bias point as  $T_c$  is reduced, and on the zero-temperature critical current ( $I_{c0}$ ). We can use (1) to substitute for the temperature term in (2a), leading to the following expression that depends only on TES current and resistance [16]:

$$\alpha = \frac{3}{2} \frac{c_R R_n}{R_0} \left( \left( 1 - \frac{R_0}{c_R R_n} \right)^{\frac{1}{3}} \left( \frac{c_I I_{c0}}{I_0} \right)^{\frac{2}{3}} - \left( 1 - \frac{R_0}{c_R R_n} \right) \right) \quad (4)$$

For fixed bias point,  $\alpha \propto (I_{c0}/I)^{2/3}$ . Via (3), we see that the current  $I$  scales as the square root of  $\kappa$  divided by resistance, so  $\alpha$  is only weakly dependent on these terms. Because the pixel with  $T_c = 76$  mK was rectangular with the longer dimension along the direction of current flow, its normal resistance was higher than that of a square device of the same area, so the resistance of the new design will be lower at a given bias point. For our TESs, this difference was measured to be approximately a factor of 1.5. The new pixel also has a larger perimeter, which increases  $\kappa$  proportionally. Combined, these two parameters increase  $\alpha$  by a factor of 1.23. This increase is beneficial for energy resolution, but at the expense of linear range. However, because the energy range of interest extends only to 1 keV, a  $\sim 20\%$  reduction in linear range relative to previous designs, which achieved good performance at 1.254 keV, should be acceptable.

Finally, we consider the critical current,  $I_{c0}$ . Experimentally, we have found that  $I_{c0}$  varies proportionally with the spacing between the normal-metal bars [16]. To achieve roughly the same critical current, our 200 μm × 200 μm pixel will have four evenly spaced normal-metal Cu bars, preserving nearly the same spacing as in the 212 μm-wide TES, which also had four normal-metal Cu bars.

We fabricated the 200 μm × 200 μm 4-bar design along with devices with smaller area to test the geometric scaling of  $C$  and  $G$  (see Fig. 1 for a summary of all TES designs). The TESs had a 1.1 μm layer of evaporated bismuth deposited on top of the bilayer to increase x-ray absorption efficiency without adding measurably to the total heat capacity [17].

### III. MEASUREMENT OF $T_c = 55$ mK DETECTORS

#### A. Measurements of TES Properties

$T_c$  for the 200 μm × 200 μm 4-bar device was 54.5 mK. Using I-V curves, we fit for  $\kappa$  and  $n$  in (3) to determine  $G = 61$  pW/K with  $n = 3.55$ . The value of  $G$  is 14% lower than expected based on the scaling measurements of the previous, higher- $T_c$  device after accounting for the difference in perimeter. Using measurements of TES impedance as a function of frequency, we fit for  $C$ ,  $\alpha$ , and  $\beta$ . We find  $C = 0.166$  pJ/K, which is 18% higher than expected based on linear scaling from previous measurements. The  $1/e$  pulse decay time constant biased at 10.5% of  $R_n$  was 280 μs. Using a linear model for the pulse shape as a function of energy, we calculate that the critically damped time constant is 87 μs, which meets the requirement for pulse decay time.

Fits to measurements of TES impedance as a function of frequency were used to determine  $\alpha$  and  $\beta$  for bias points of 8–25%  $R_n$  at a bath temperature of 35 mK. Rather than comparing values of  $\alpha$  directly between devices, we compare the ratio  $\alpha/\sqrt{(1+2\beta)}$ . Generally,  $\alpha$  varies rapidly throughout the transition, so a failure to exactly match biasing conditions between devices can cause large differences in  $\alpha$ . The ratio  $\alpha/\sqrt{(1+2\beta)}$  varies slowly through the transition and has the added benefit that it is inversely proportional to the energy resolution. In the  $T_c = 76$  mK device described in Section II.C,  $\alpha/\sqrt{(1+2\beta)} = 70.6$  at 10%  $R_n$ . For the new device, based on the scaling arguments described in the previous section, we expected this ratio to increase by a factor of 1.23. We measured  $\alpha/\sqrt{(1+2\beta)} = 81.2$  at 9.5%  $R_n$ , a factor of 1.15 increase. This increase in  $\alpha/\sqrt{(1+2\beta)}$ , coupled with a reduction in  $T_c$  from 76 mK to 54.5 mK, means the energy resolution should improve from the previous result.

#### B. X-Ray Spectra

An X-ray tube source was used to fluoresce a target comprised of magnesium and aluminum, which produced  $K\alpha$  emission lines from the two elements at 1.254 keV and 1.487 keV, respectively. Broadening of the  $K\alpha$  features beyond their natural line widths [18]–[21] is caused by the energy resolution of our TES.

The 200 μm × 200 μm 4-bar pixel achieves  $\Delta E = 0.87$  eV ± 0.07 eV FWHM resolution at 1.254 keV (Mg  $K\alpha$ ) and 1.29 eV ± 0.05 eV at 1.487 keV (Al  $K\alpha$ ). The difference is due to non-linearity of the TES response at higher energy. Our test array also included a 180 μm × 180 μm 3-bar pixel. If  $C$  had scaled with temperature as expected, this pixel would have had a dynamic range that was too small to expect good performance at  $E > 1$  keV. Instead, this pixel performed even better than its larger counterpart:  $\Delta E = 0.75$  eV ± 0.07 eV at 1.254 keV and 0.94 eV ± 0.03 eV at 1.487 keV (see Fig. 2).

A fluoresced Cu target produced Cu  $L\alpha$  emission at 929.7 eV. Because L-line fluorescence is relatively inefficient and transmission through the cryostat windows falls sharply in this energy range, we were unable to collect sufficient data to fit a spectral-line shape. For the 180 μm × 180 μm 3-bar pixel, the flux was too dim to identify the emission line at all. However, for the 200 μm × 200 μm 4-bar pixel we saw sufficient flux to make an averaged pulse shape of Cu  $L\alpha$  photons, construct an optimal filter, and compute the energy resolution expected based on the signal-to-noise ratio. This calculation suggests that the energy



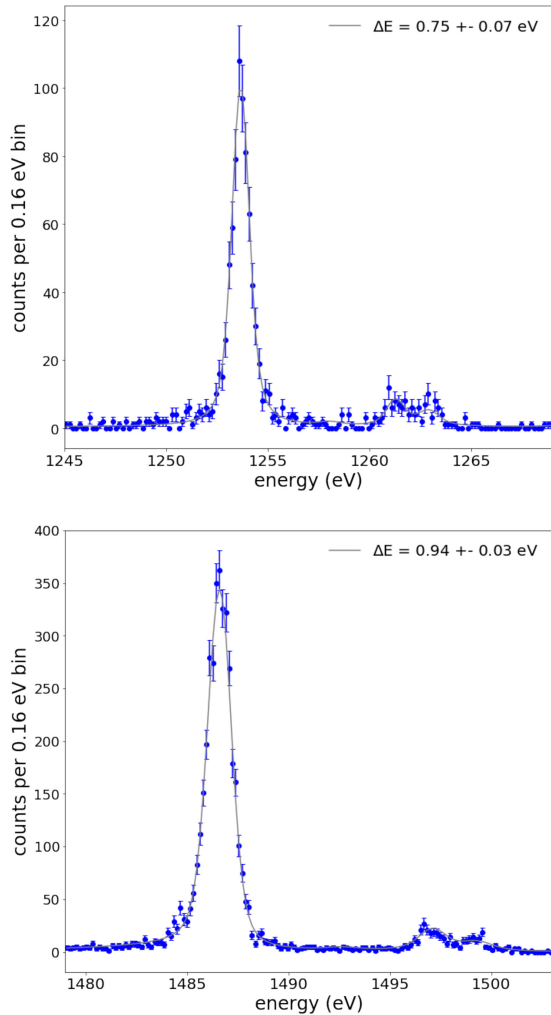


Fig. 2. X-ray fluorescence spectra measured by a  $180 \mu\text{m} \times 180 \mu\text{m}$  3-bar TES, biased at 9.5% Rn with  $T_{\text{bath}} = 35$  mK. (Top) The detector resolution at 1.254 keV (Mg Ka emission) is  $\Delta E = 0.75 \text{ eV} \pm 0.07 \text{ eV}$  FWHM. (Bottom) The resolution at 1.487 keV (Al Ka emission) is  $\Delta E = 0.94 \text{ eV} \pm 0.03 \text{ eV}$  FWHM.

resolution expected for the  $200 \mu\text{m} \times 200 \mu\text{m}$  4-bar pixel is 0.72 eV at 929.7 eV, versus 0.85 eV measured at 1.254 keV. Some improvement at lower photon energies is expected since the TES response is somewhat non-linear at 1.254 keV; the pulse height changed only 75% as quickly with energy as would be expected for a perfectly linear detector.

#### IV. DESIGN OF $\Delta E = 0.5$ eV DETECTORS

The design specification for the LCLS-II spectrometer is  $\Delta E_{\text{FWHM}} = 0.5$  eV resolution for energies below 1 keV. The current best result of  $\Delta E = 0.75$  eV at 1.254 keV must be improved by 33%. Given that the energy range of interest extends only to 1 keV, we can sacrifice some linear range by reducing the ratio  $CT/\alpha$ . For example, if we reduce the range by the ratio 1/1.254 to about 80%, the energy resolution will improve as the square root of this ratio, or 10%.

The LCLS-II spectrometer will be cooled by a dilution refrigerator to a base temperature of about 8 mK, so we can lower

$T_c$ . A  $T_c$  of 30 mK, coupled with the small reduction in linear range described above will improve the energy resolution from 0.75 eV to 0.49 eV. This meets the requirement for LCLS-II.

As before, the pixel design should be modified to offset the reduction in heat capacity due to lowering the operating temperature. At 30 mK, the operating temperature is 54.5% of that of the  $T_c = 55$  mK design, so we expect  $C \times T$  for the new pixel to be 29.7% of  $C \times T$  for the 55 mK pixel. The target  $CT/\alpha$  was 80% of the value at 55 mK, so there is considerable margin to increase  $C$  or decrease  $\alpha$ . We could decrease  $\alpha$  by adding normal metal bars, but generally it is more beneficial to increase  $C$  by making the TES area larger and so provide more collecting area for incident photons. Therefore, based on current results, a  $220 \mu\text{m} \times 220 \mu\text{m}$  TES with  $T_c = 30$  mK is expected to achieve the target energy resolution of 0.5 eV at 1 keV.

This is contingent on the assumption that the heat capacity of the TES will scale approximately linearly with temperature, as is generally expected in metals where the conduction electrons are the dominant contribution to the heat capacity. However, as discussed in Section III A, we observed that the measured heat capacity at  $T_c = 54.5$  mK was about 18% larger than expected based on scaling from measurements of  $T_c = 76$  mK devices. Presently, the origin of this discrepancy is not understood. Some groups have reported measurements of excess heat capacity in copper at millikelvin temperatures [22], [23]. Alternatively, we have previously observed that process variability during fabrication can occasionally introduce excess heat capacity. Fabricating and testing more devices at  $T_c = 55$  mK and lower will help identify the source of the excess. If the excess is found to persist (or grow) at lower temperatures, then the pixel size can be adjusted accordingly.

#### V. CONCLUSION

We have demonstrated a  $180 \mu\text{m} \times 180 \mu\text{m}$  3-bar Mo/Cu bilayer TES with  $T_c = 55$  mK that achieves  $\Delta E = 0.75$  eV FWHM at 1.254 keV and 0.94 eV at 1.487 keV, and a  $200 \mu\text{m} \times 200 \mu\text{m}$  4-bar TES that achieves  $\Delta E = 0.87$  eV FWHM at 1.254 keV and 1.29 eV at 1.487 keV. The size, shape, and normal-metal bar design were chosen via two-fluid model principles to understand the change in the sharpness of the transition, parameterized by  $\alpha$ , with temperature, current, and critical current. Although the heat capacity of the TESs was found to be higher than expected based on scaling from higher- $T_c$  devices, the new devices still represent a substantial improvement in resolution over previous detectors, enabled by lowering  $T_c$  and the concomitant increase in  $\alpha$ . Operation at lower  $T_c$  also allows a larger area pixel for increased collecting area with the same dynamic range. Furthermore, the result provides a basis for straightforward changes to the pixel design and  $T_c$  to achieve the 0.5 eV FWHM energy resolution specified for the LCLS-II soft x-ray spectrometer.

#### ACKNOWLEDGMENT

The authors are grateful for useful technical discussions with the larger team contributing to the soft X-ray TES spectrometer being developed for the LCLS-II.

## REFERENCES

- [1] J. N. Ullom *et al.*, "Transition-edge sensor microcalorimeters for x-ray beamline science," *Synchr. Rad. News*, vol. 27, no. 4, pp. 24–27, Jul. 2014.
- [2] J. N. Ullom and D. A. Bennett, "Review of superconducting transition-edge sensors for x-ray and gamma-ray spectroscopy," *Supercond. Sci. Tech.*, vol. 28, no. 8, Jul. 2015, Art. no. 084003.
- [3] W. B. Doriese *et al.*, "A practical superconducting-microcalorimeter X-ray spectrometer for beamline and laboratory science," *Rev. Sci. Inst.*, vol. 88, no. 5, May 2017, Art. no. 053108.
- [4] C. J. Titus *et al.*, "L-edge spectroscopy of dilute, radiation-sensitive systems using a transition-edge-sensor array," *J. Chem. Phys.*, vol. 147, no. 21, Dec. 2017, Art. no. 214201.
- [5] D. Li *et al.*, "TES X-ray Spectrometer at SLAC LCLS-II," *J. Low Temp. Phys.*, vol. 193, no. 5–6, pp. 1287–1297, Sep. 2018.
- [6] D. A. Bennett, D. S. Swetz, R. D. Horansky, D. R. Schmidt, and J. N. Ullom, "A two-fluid model for the transition shape in transition-edge sensors," *J. Low Temp. Phys.*, vol. 167, no. 3–4, pp. 102–107, May 2012.
- [7] K. D. Irwin, G. C. Hilton, D. A. Wollman, and J. M. Martinis, "Thermal-response time of superconducting transition-edge microcalorimeters," *J. Appl. Phys.*, vol. 83, no. 8, pp. 3978–3985, Apr. 1998.
- [8] W. Holmes, J. M. Gildemeister, P. L. Richards, and V. Kotsubo, "Measurements of thermal transport in low stress silicon nitride films," *Appl. Phys. Lett.*, vol. 71, no. 18, pp. 2250–2252, May 1998.
- [9] A. Woodcraft, R. Sudiwala, E. Wakui, R. Bhatia, J. Bock, and A. Turner, "Thermal conductance measurements of a silicon nitride membrane at low temperatures," *Phys. B*, vol. 284–288, pp. 1968–1969, Jul. 2000.
- [10] J. E. Sadleir, S. J. Smith, S. R. Bandler, J. A. Chervenak, and J. R. Clem, "Longitudinal proximity effects in superconducting transition-edge sensors," *Phys. Rev. Lett.*, vol. 104, Jan. 2010, Art. no. 047003.
- [11] A. Kozorezov *et al.*, "Modelling the resistive state in a transition edge sensor," *Appl. Phys. Lett.*, vol. 99, 2011, Art. no. 063503.
- [12] S. J. Smith *et al.*, "Implications of weak-link behavior on the performance of Mo/Au bilayer transition-edge sensors," *J. Appl. Phys.*, vol. 114, Aug. 2013, Art. no. 074513.
- [13] J. E. Sadleir *et al.*, "Proximity effects and nonequilibrium superconductivity in transition-edge sensors," *Phys. Rev. B*, vol. 84, Nov. 2011, Art. no. 184502.
- [14] D. A. Bennett, D. R. Schmidt, D. S. Swetz, and J. N. Ullom, "Phase-slip lines as a resistance mechanism in transition-edge sensors," *Appl. Phys. Lett.*, vol. 104, Jan. 2014, Art. no. 042602.
- [15] W. J. Skocpol, M. R. Beasley, and M. Tinkham, "Phase-slip centers and nonequilibrium processes in superconducting tin microbridges," *J. Low Temp. Phys.*, vol. 16, no. 1–2, pp. 145–167, 1974.
- [16] K. M. Morgan *et al.*, "Dependence of transition width on current and critical current in transition-edge sensors," *Appl. Phys. Lett.*, vol. 110, no. 21, May 2017, Art. no. 212602.
- [17] D. Yan *et al.*, "Eliminating the non-Gaussian spectral response of X-ray absorbers for transition-edge sensors," *Appl. Phys. Lett.*, vol. 111, 2017, Art. no. 192602.
- [18] C. Klauber, "Magnesium  $K\alpha$  x-ray line structure revisited," *Appl. Surf. Sci.*, vol. 70–71, pp. 35–39, Jun. 1993.
- [19] S. J. Lee *et al.*, "Fine pitch transition-edge sensor X-ray microcalorimeters with sub-eV energy resolution at 1.5 keV," *Appl. Phys. Lett.*, vol. 107, Dec. 2015, Art. no. 223503.
- [20] D. A. Wollman *et al.*, "Superconducting transition-edge-microcalorimeter X-ray spectrometer with 2 eV energy resolution at 1.5 keV," *Nucl. Instrum. Meth. A*, vol. 444, no. 1–2, pp. 145–150, Apr. 2000.
- [21] J. Schweppe, R. D. Deslattes, T. Mooney, and C. J. Powell, "Accurate measurement of Mg and Al  $K\alpha_{1,2}$  X-ray energy profiles," *J. Electron Spectrosc.*, vol. 67, no. 3, pp. 463–478, Jun. 1994.
- [22] G. J. Sellers and A. C. Anderson, "Calorimetry below 1 K: The specific heat of copper," *Rev. Sci. Inst.*, vol. 45, pp. 1256–1259, Jun. 1974.
- [23] K. Gloos *et al.*, "The bayreuth nuclear demagnetization refrigerator," *J. Low Temp. Phys.*, vol. 73, no. 1–2, pp. 101–136, Apr. 1988.